Peer-reviewed version available at Catalysts 2019, 9, 815; doi:10.3390/catal9100815

Article

Reactive Fe-O-Ce Sites in Ceria Catalysts for Soot Oxidation

Boyu Li [1], Abhishek Raj [2], Eric Croiset [1] and John Z. Wen [2,*]

[1] Department of Chemical Engineering, University of Waterloo, 200 University Avenue West, Waterloo, ON N2L3G1, Canada
[2] Department of Mechanical & Mechatronics Engineering, University of Waterloo, 200 University Avenue West, Waterloo, ON N2L3G1, Canada
* Correspondence: ecroiset@uwaterloo.ca; Tel.: 1-519-8884567 x 32295

Abstract: This study investigates the role of oxygen vacancy on Fe-doped CeO_2 catalyst activity for soot oxidation. The oxygen vacancy was assessed through Ce^{3+} content. The Fe content was varied between 0 and 30% for two catalyst preparation methods, co-precipitation (CP) and solution combustion synthesis (SCS). X-ray photoelectron spectroscopy indicates that ceria exists as both Ce^{4+} and Ce^{3+}, while iron is present only as Fe^{3+}. The catalyst's activity was evaluated by ignition (T10) and combustion (T50) temperatures using thermogravimetric analysis. Optimum Fe contents yielding the highest activity were found to be 10% and 5% for CP and SCS catalysts, respectively. The surface area and morphology have shown moderate effect on catalyst activity, because catalytic soot oxidation involves solid-solid contact. More importantly, regardless of the fabrication method, it was found that Ce^{3+} content, which is closely related to oxygen vacancies, plays the most important role in affecting the catalyst activity.

Keywords: Soot Oxidation; Catalytic; Heterogeneous catalysis; Oxygen vacancies; Iron doped ceria catalyst; Ceria

1. Introduction

PM (consisting primarily of soot) can cause serious environmental and health problems, such as lung cancer [1-3]. PM emission can be controlled through processing the exhaust gas through a diesel particulate filters (DPF). DPF with a monolithic geometry have been used to capture and oxidize fine carbon particles [4]. The desired temperature of soot combustion is above 600°C, but the temperature of exhaust gas is around 200-500°C [5-7]. It is necessary to introduce catalysts to effectively decrease the soot oxidation temperature and improve the reactor efficiency. Usually, the catalyst is coated on the monolith wall of the DPF [4-11]. After a period of soot deposition, a pressure drop may occur through the DPF, making it necessary to regenerate the DPF periodically [11].

The desired catalysts for soot oxidation should have high activity and suitable stability but low cost, which makes ceria-based catalyst particularly attractive [15]. Ceria-based catalysts have been applied on DPF to study their catalytic activity for soot oxidation [15, 18, 19]. Ceria has been found to act as an active oxygen producer to promote the formation of reactive oxygen species and transfer them to soot-catalyst interface to oxidize soot, which is described in the active oxygen-assisted oxidation mechanism [12, 15]. The oxygen species can be transferred between the oxidized state Ce^{4+} and reduced state Ce^{3+} [1, 2, 20-22], thus forming oxygen vacancies through Ce^{4+} to Ce^{3+} reduction, and absorbing gaseous oxygen via Ce^{3+} to Ce^{4+}.

The activity of ceria-based catalysts can be further improved through doping other metal additives into the ceria lattice, in order to enhance the oxygen storage capability (OSC) and oxygen mobility [15, 22]. Transition metal doping has been reported to produce more active sites over the catalyst surface and promote catalytic soot oxidation [20, 23-25]. Iron, in particular, is prominent

Peer-reviewed version available at Catalysts 2019, 9, 815; doi:10.3390/catal9100815

because it can improve the catalyst activity due to its good redox ability - the oxygen species can alternate between Fe^{3+} and Fe^{2+} [2, 15, 26]. The mechanism of iron doped ceria catalysts has been investigated by Zhang et al. [20] indicating that the redox cycle of iron played an important role in this reaction. Fe^{3+} can provide its bonded active oxygen to oxidize soot, along with its reduction to Fe^{2+}. Fe^{2+} can then be re-oxidized to Fe^{3+} with the interaction of Ce [15, 20]. The number of active Fe-O-Ce sites can vary due to different ratios of iron doping, as iron doping can distort the fluorite lattice and create oxygen vacancies to varying degrees. Thus, the ratio of iron doping in ceria affects the catalyst activity and need be optimized with reaction conditions.

As the catalytic soot oxidation is a surface sensitive reaction, the contact points between soot and catalyst particles have a great impact on activity [1]. Nano-sized materials result in a high surface-to-volume ratio and make their chemical and physical properties more size and shape dependent [27-29]. More specifically, the quantum size effects and higher surface areas make these nanostructured catalysts possess more potential contact points between soot and catalyst particles while their meso-scale pores (with diameters between 2 and 50 nm) can promote the oxygen diffusion through catalysts [27]. In order to enhance the interactions between soot and catalyst, different morphologies of ceria-based catalysts have been fabricated by a number of preparation methods [30-36]. It is found that different morphologies exhibit distinct catalytic activity, which is strongly dependent on their physical and chemical surface properties [15]. Among these preparation methods, co-precipitation (CP) method has been widely used for catalyst preparation due to the formation of higher surface area and smaller crystal size [20]. Alternatively, solution combustion synthesis (SCS) is a time effective and energy saving method to produce nano-sized porous catalysts [37]. Herein, these two preparation methods have been chosen in this study to investigate the morphologies influence on catalyst activity.

Different iron doping ratios and morphologies would change the surface properties and oxygen vacancies of catalysts, which has influence on catalyst activity [38]. Kattal et al. found that increasing oxygen vacancies induces more active oxygen for CeO_2–La_2O_3 catalyst [39]. Pr, La, Tb doped CeO_2 catalyst were studied for methane steam reforming, revealing that increased oxygen storage capacity contributes to higher activity [40]. Oxygen vacancy of Ag-doped perovskite catalysts was found to be the primary intermediates for the NO oxidation reaction [41]. Zr doped CeO_2 catalyst showed positive relation between oxygen vacancy concentration and catalyst activity for dimethyl carbonate synthesis [42]. The above-mentioned studies showed a relation between oxygen vacancy and catalyst activity. However, the effect of oxygen vacancy on soot oxidation by altering the catalyst morphologies along with different Fe doping ratios is still poorly understood. Therefore, this study aims at investigating the role of oxygen vacancy on catalyst activity through varying the Fe doping ratio and tailored catalyst morphology.

2. Results and Discussion

2.1. Characterization

The crystal structure of all catalysts was studied by XRD. The XRD patterns of iron doped cerium oxide catalysts prepared by SCS and CP methods are depicted in Figure 1. The main diffraction peaks could be attributed to (111) (200) (220) (311) (222) (400) (331) (420) planes, referring to a typical face-centered cubic fluorite structure matching the spectra for pure cerium oxide (JCPDS NO. 34-0394) [43]. The characteristic peaks shifted to higher 2θ diffraction angle with iron doping and no peaks of Fe_2O_3 was observed, suggesting the uniform incorporation of iron into cerium oxide lattice and the formation of solid solution, thus the catalyst could be represented by Fe_xCe_{100-x} [2, 26, 39, 44]. The absence of characteristic peaks of iron oxide could also result from the absence of iron oxide on the surface or from crystal being too small to be detected by XRD.

Peer-reviewed version available at Catalysts 2019, 9, 815; doi:10.3390/catal9100815

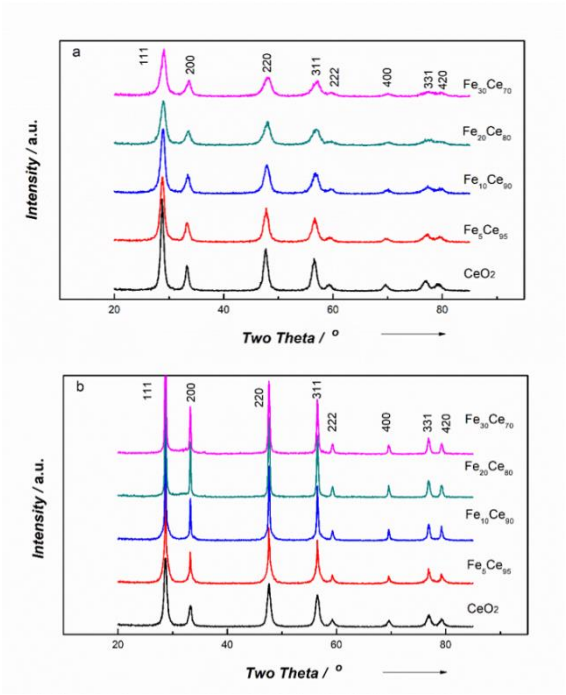

Figure 1. Powder X-ray diffraction patterns of (a) Co-precipitation method, (b) Solution combustion synthesis method

The textural properties of catalysts are listed in Table 1; the crystal size was calculated by using the Scherrer equation, while the unit lattice parameter was calculated by Bragg's law using the strongest peak (111). From Table 5.1, it is clear that CP catalysts lead to smaller crystal size than for SCS catalysts. In addition, compared to pure ceria, iron doping results in smaller crystal size for CP catalyst, but in much higher crystal size for SCS catalyst. Table 1 also shows that the lattice parameter slightly decreases with more iron doping. This is because of the smaller iron atoms (Fe^{3+}-0.64 Å, Fe^{2+}-0.74 Å) substituting larger ceria sites (0.97 Å) in the lattice to form Ce-Fe-O solid solution [26]. These results also indicated the incorporation of iron into ceria lattice.

Table 1. Textural properties of as-derived catalysts

Catalyst	Crystal size [nm]	Lattice parameter [Å]	S_{BET} [m^2g^{-1}]	Pore size [nm]
CeO_2-CP	11.71	5.38	73	2.46
Fe_5Ce_{95}-CP	9.11	5.36	87	3.48
$Fe_{10}Ce_{90}$-CP	8.63	5.34	94	3.49
$Fe_{20}Ce_{80}$-CP	7.96	5.33	87	5.60
$Fe_{30}Ce_{70}$-CP	7.89	5.32	65	3.51
CeO_2-SCS	13.33	5.39	38	3.63
Fe_5Ce_{95}-SCS	30.59	5.38	39	4.61
$Fe_{10}Ce_{90}$-SCS	31.53	5.37	20	3.66
$Fe_{20}Ce_{80}$-SCS	32.79	5.37	3	4.56
$Fe_{30}Ce_{70}$-SCS	34.15	5.37	2	3.82

As shown in Table 1, catalysts made by CP method reveal higher surface area than those made by SCS method. $Fe_{10}Ce_{90}$- CP and Fe_5Ce_{95}-SCS yielded the highest specific surface area within their preparation method, and $Fe_{10}Ce_{90}$-CP showed the largest surface area (94 m^2g^{-1}) among all. Accordingly, introduction of iron enlarged the surface area of CP catalyst. For SCS catalysts, only 5% iron doping showed slight increase of surface area compared to pure CeO_2, but other ratio doping

Peer-reviewed version available at Catalysts 2019, 9, 815; doi:10.3390/catal9100815

led to a surface area decrease. It was also noticed that the surface area greatly dropped with more than 20% of iron doping, especially for SCS method. The pore diameters of both CP and SCS catalysts are around 3-5 nm.

SEM was performed to explore the surface morphologies of catalysts. In Figure 2, both pictures clearly show the nanoparticle morphologies: the CP method produced uniform spherical morphology with some agglomeration, while catalyst made by SCS method reported a spongy structure. The spherical morphology for CP method was a result of precipitants' nucleation, and these small particles yielded higher surface area. The foamy and highly porous spongy structure is a more unpredictable structure made from SCS method, which was due to the combustion procedure- the reacting precursor releasing lots of gaseous products in a short time. Moreover, these bigger openings got from this morphology can be large enough (around 250 nm diameter) for soot particle (typical size around 25 nm) to penetrate, thus creating more contact points between soot and catalyst particles.

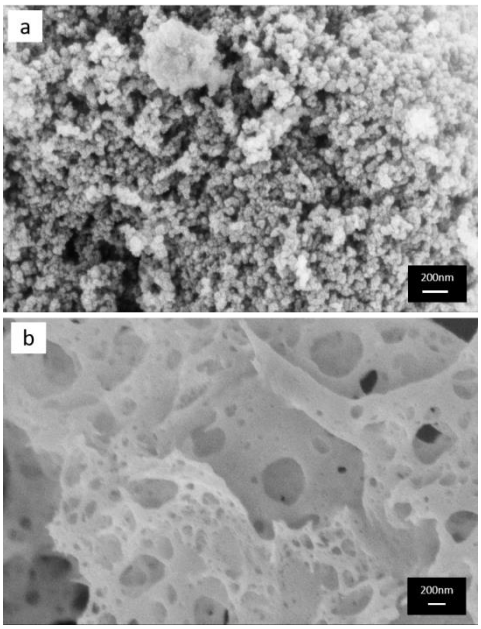

Figure 2. FE-SEM images of (a) Co-precipitation method, (b) Solution combustion synthesis method

XPS analysis was undertaken to study the surface properties of catalysts in terms of their oxidation state and surface oxygen vacancies. Figure 3 shows the Ce 3d spectra of all catalysts. The Ce 3d spectra could be curve fitted into eight peaks corresponding to the spin-orbit splitting of Ce $3d_{5/2}$ and Ce $3d_{3/2}$, which were labelled as "u" and "v" respectively [45]. The peaks labelled as v0, v2, v3, u0, u2, u3 with binding energy (BE) around 882, 888, 898, 900, 907, 916 eV correspond to the Ce^{4+} species and peaks labelled as v1, u1 with binding energy of 884 and 902 eV are ascribed to Ce^{3+} species. The analysis of XPS spectra suggested that Ceria existed as both Ce^{3+} and Ce^{4+}, but primarily in Ce^{4+} state. When Ce^{4+} transferred to Ce^{3+}, an oxygen vacancies associated with Ce^{3+} could be generated to potentially absorb oxygen and provide it for soot oxidation. Therefore, the existence of Ce^{3+} becomes important to indicate the generation of oxygen vacancies [2, 26]. The calculations of integrated peak areas was used to get a quantitative analysis of a selected element. In this way, the ratio of Ce^{3+} area to total area including Ce^{3+} and Ce^{4+} was applied to estimate the ratio of Ce^{3+}; the result are given in Table 2. From Table 2, all Ce^{3+} percentage are around 20%, CP catalysts are between 19% - 25%, and SCS catalysts are between 17% - 27%. Ce^{3+} content has the similar trend for both CP and SCS catalysts, which is Ce^{3+} goes up to a maximum value then goes down. The maximum Ce^{3+} value for CP catalysts is 24.9% with 10% iron doping, and is 27.1% with 5% iron doping for SCS catalysts. Among all catalysts, Fe_5Ce_{95}-SCS gives the highest Ce^{3+} percentage, higher than $Fe_{10}Ce_{90}$-CP. Therefore, it can be deducted that Fe_5Ce_{95}-SCS has the highest concentration of oxygen vacancies.

Peer-reviewed version available at Catalysts 2019, 9, 815; doi:10.3390/catal9100815

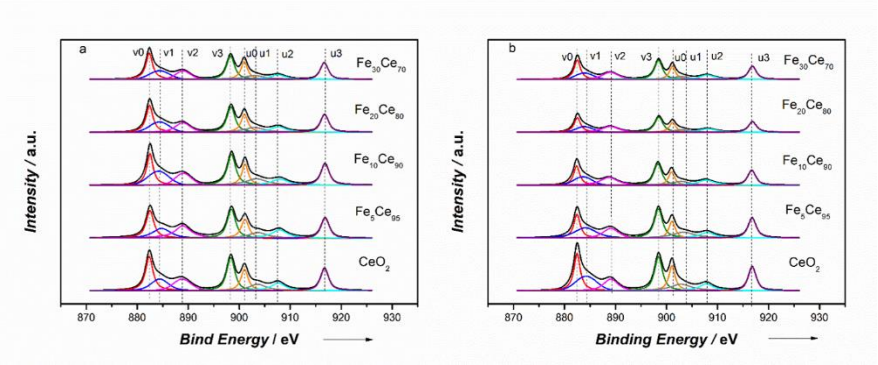

Figure 3. XPS spectra of Ce3d (a) Co-precipitation method, (b) Solution combustion synthesis method

The Fe 2p spectra in Figure 4 showed the characteristic Fe $2p_{3/2}$ and Fe $2p_{3/1}$ peaks at binding energy of 711 and 724 eV, respectively. Two satellites peaks at 718 and 733 eV were slightly distinguished. These peaks indicated the existence of Fe^{3+}. The binding energy of Fe 2p decreased with more iron doping, further confirming that Fe^{3+} incorporated into CeO_2 lattice and formed a solid solution, as shown by XRD results.

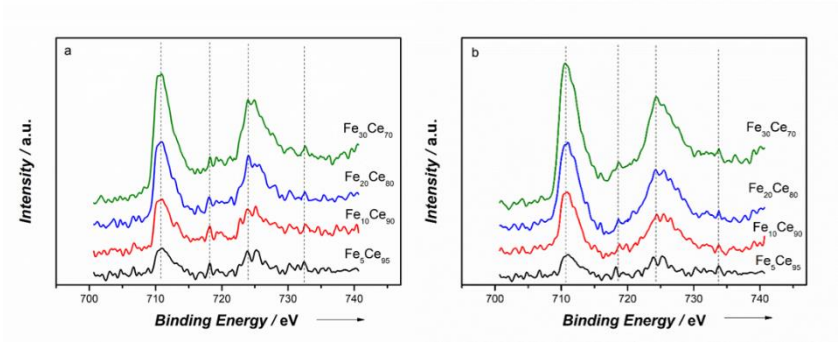

Figure 4. XPS spectra of Fe2p (a) Co-precipitation method, (b) Solution combustion synthesis method

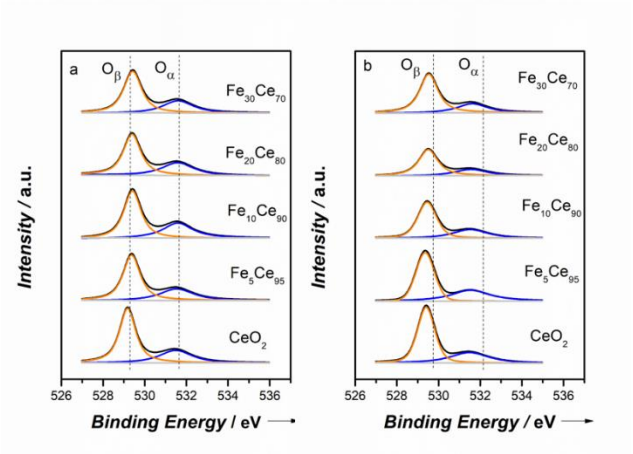

Figure 5. XPS spectra of O1s (a) Co-precipitation method, (b) Solution combustion synthesis method

The O1s spectra showed two distinct peaks in Figure 5. The peak at higher binding energy (~531.7 eV) referred to the surface oxygen species O_α, and the peak at lower binding energy (~529.5 eV) is attributed to the lattice oxygen O_β [33]. As Fe is added into CeO_2, the main peak O_β shifted to higher binding energy, suggesting the chemical environment of lattice oxygen changed due to incorporation of Fe [46]. The surface oxygen species O_α are critical for soot oxidation because they can become active and react with soot particles. The ratio of surface oxygen concentration to lattice oxygen concentration can be estimated by the integrated peak areas of O_α and O_β, and the results

Peer-reviewed version available at Catalysts 2019, 9, 815; doi:10.3390/catal9100815

are shown in Table 2. For CP method, O_α percentage - $O_\alpha/(O_\alpha+O_\beta)$ increased to a maximum point (60%) at 10% iron doping, and then decreased. SCS catalysts showed similar behavior, where it reached a maximum value (64%) at 5% iron doping. Among all, Fe_5Ce_{95} –SCS led to the highest surface oxygen concentration. These results agree well with concentration percentage of Ce^{3+}.

Table 2. Curve fitting results of Ce3d and O1s on obtained catalysts

Catalyst	Preparation method	Ce^{3+} content [%]	O_α content [%]	I_{596}/I_{463}
CeO_2	CP	20.1	31.5	0.023
	SCS	24.5	33.3	0.028
Fe_5Ce_{95}	CP	19.7	32.8	0.037
	SCS	27.1	39.0	0.032
$Fe_{10}Ce_{90}$	CP	24.9	37.5	0.029
	SCS	20.4	33.8	0.029
$Fe_{20}Ce_{80}$	CP	21.4	35.5	0.038
	SCS	17.1	29.1	0.021
$Fe_{30}Ce_{70}$	CP	20.5	33.3	0.013
	SCS	16.9	28.1	0.011

The Raman spectroscopy was conducted to study the oxygen vacancies and active sites within the catalysts. Figure 6 shows the Raman spectra of Fe_xCe_{100-x} catalysts made by CP and SCS methods. The prominent band at ~463cm^{-1} could be assigned to the first order scattering F2g symmetric oxygen active mode around Ce^{4+} with a CeO_2 fluorite structure [47], which is in agreement with the XRD and XPS results. All catalysts spectra are identical to that of pure CeO_2, further indicating that iron has been incorporated into the CeO_2 lattice. Compared to the Raman spectra of pure CeO_2, the F2g band shifted to lower frequency and broadened with an increase in iron doping, suggesting the lattice distortion due to the incorporation of iron into CeO_2 fluorite lattice [35]. The intensity (I) of Raman spectra decreased with increasing iron doping, indicating the structure change due to Fe incorporation and lower ceria content [26]. No peaks of Fe_2O_3 were observed, which is possible due to the much weaker bands of Fe_2O_3 than CeO_2 and the formation of solid solution. Two weak bands at ~261 and 596 cm^{-1} were characteristic bands of second order scattering, which can represent the oxygen vacancies in the lattice [20]. The low intensity of oxygen vacancies showed in Raman spectra was because the sample was not outgassed, the intensity would be higher if the sample was outgassed at high temperature [44].

Peer-reviewed version available at Catalysts 2019, 9, 815; doi:10.3390/catal9100815

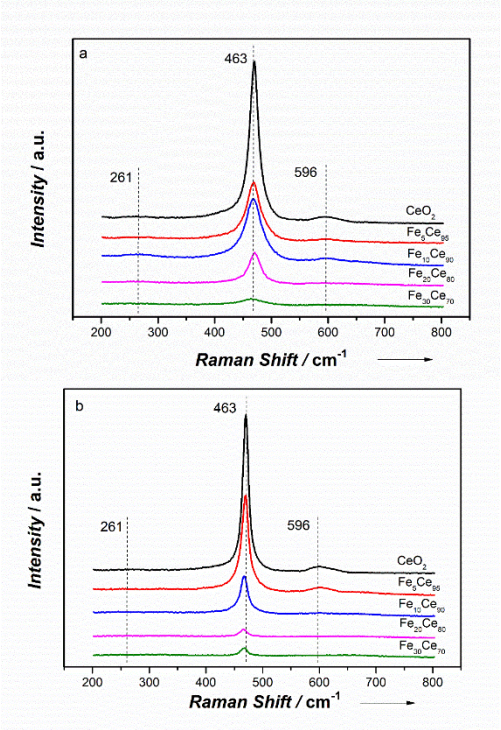

Figure 6. Raman spectra of (a) Co-precipitation method, (b) Solution combustion synthesis method

The 596 cm^{-1} band exhibits the oxygen vacancies caused by Ce^{3+}, thus the value of I_{596}/I_{463} (as shown in Table 2) becomes important to evaluate the oxygen vacancies or amount of defects in the catalysts. Catalysts made by the two methods (CP and SCS) showed similar trend of I_{596}/I_{463} with increasing iron content, that is rise first to reach a maximum and then drop down. This is because Fe prefers to occupy Ce sites in CeO_2, thus the oxygen vacancy concentration increases with more Fe doping. But when the amount of Fe exceeded a critical value, Fe turned into interstitial in CeO_2 lattice, thus decreasing oxygen vacancy concentration [48]. The results showed that $Fe_{10}Ce_{90}$-CP and Fe_5Ce_{95}-SCS reached optimum I_{596}/I_{463} value within their preparation method. Fe_5Ce_{95}-SCS obtained the maximum I_{596}/I_{463} value, indicating highest oxygen vacancies.

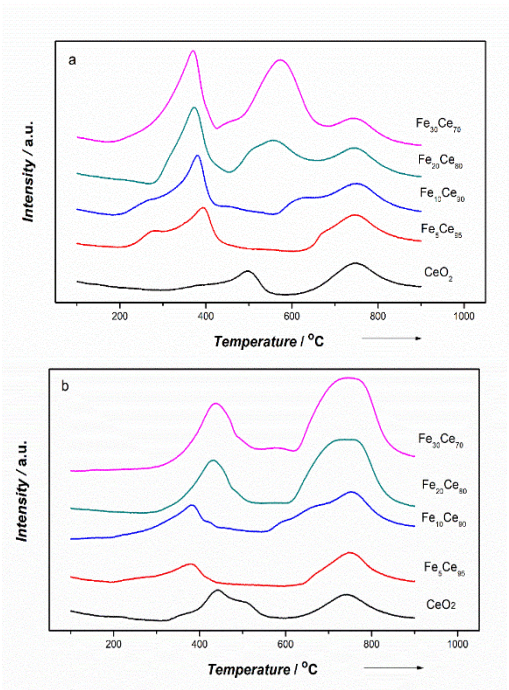

Figure 7. H2-TPR results of (a) Co-precipitation method, (b) Solution combustion synthesis method

Peer-reviewed version available at Catalysts 2019, 9, 815; doi:10.3390/catal9100815

H_2-TPR was applied to investigate catalysts' reducibility. As shown in Figure 7, pure CeO_2 had two main H_2 consumption peaks. The peak at lower temperature (500°C for CP and 440°C for SCS) corresponded to reduction of surface oxygen of ceria, and the other peak at higher temperature (~750°C) is attributed to reduction of bulk oxygen of ceria. Pure CeO_2 made by SCS method had a better reducibility than that prepared by CP method. For Fe-doped ceria CP catalysts, the reduction peak of surface oxygen shifted towards lower temperature with increase of Fe doping, indicating that the Ce-O bond weakened and the mobility of surface oxygen improved. For SCS catalysts, the peaks of surface oxygen reduction shifted to lower temperature with 5% and 10% Fe doping (378°C and 384°C, respectively). But when the doping ratio was higher than 20%, the peak shifted to higher temperature and remained similar to pure CeO_2, meaning that reducibility can only be improved by low Fe doping (<10%). Additionally, these peaks of surface oxygen reduction for both CP and SCS catalysts were broader and with higher intensity as more Fe is incorporated.

However, the temperature of bulk oxygen reduction remained almost unchanged for CP and SCS catalysts. This is because lattice oxygen needed to be transferred to the surface before being reduced, and adding Fe did not change the reducibility of bulk oxygen. . It is noticed that the peaks of SCS bulk oxygen reduction became higher and broader when increasing Fe doping, suggesting that more releasable lattice oxygen could be transferred to surface oxygen [15]. For $Fe_{20}Ce_{80}$-CP and $Fe_{30}Ce_{70}$-CP, an additional peak around 550°C was observed, which could be attributed to reduction of iron oxide species. According to the literature, Fe_2O_3 normally showed two steps reduction: Fe_2O_3 to Fe_3O_4 around 385-425°C and Fe_3O_4 to Fe at 590-745°C, respectively [20]. Hence, the additional peak shown on $Fe_{20}Ce_{80}$-CP and $Fe_{30}Ce_{70}$-CP catalyst could be assigned to the iron oxide reduction. This means that some isolated iron oxide species can exist when Fe doping ratio is above 20%. The reason for XRD not detecting single phase iron oxide was because of the very limited amount of these iron oxide and XRD only detect the surface properties, but iron oxide could be inside the crystal structure. Herein, for higher ratio of iron doping, the CP catalysts had co-existence of solid solution and some iron oxide phase. But for SCS method catalysts, no reduction peak of iron oxide was observed, which might be due to the absence of iron oxide or not detecting the limited amount of iron oxide.

2.2. Activity study

TGA experiments were carried out to investigate the catalyst activity for soot oxidation. Tight contact condition was used to study the influence of iron doping ratio and morphology on catalyst activity. The result of soot conversion as a function of temperature is shown in Figure 8. Tight contact condition was used to explore the intrinsic activity of the catalysts because soot and catalysts were ground together to produce more contact points [22]. The activity of catalyst was evaluated by the ignition temperature (T10) and combustion temperature (T50). T10 and T50 for tight contact condition are summarized in Table 3. For comparison, non-catalytic soot oxidation was also conducted at the same reaction conditions.

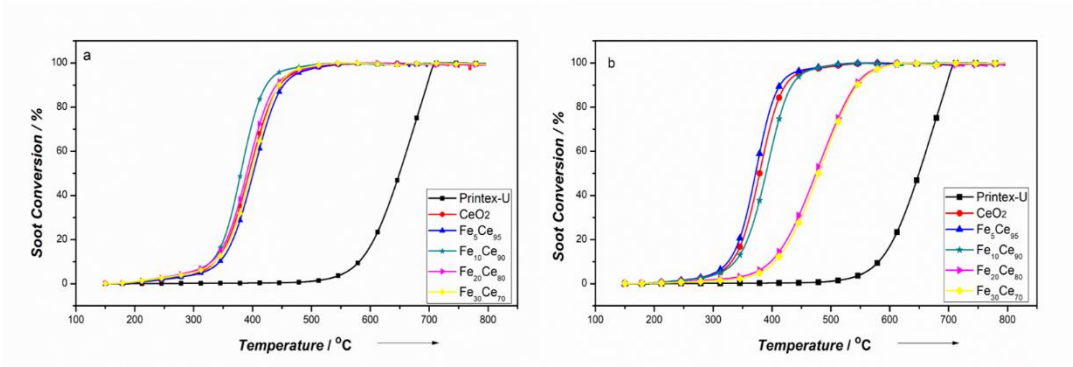

Figure 8. Soot conversion of tight contact condition: (a) Co-precipitation method, (b) Solution combustion synthesis method

Peer-reviewed version available at Catalysts 2019, 9, 815; doi:10.3390/catal9100815

From Figure 8, it is obvious that soot oxidation temperatures decreased significantly when adding catalyst compared to non-catalytic soot oxidation. Different iron doping ratios and morphologies have distinct effects on catalyst activity. CP and SCS catalysts showed similar trend of T10 and T50 with different iron doping ratio, which decreased first to a threshold then began to increase. The minimum temperature in T10 and T50 for CP catalysts are T10~328°C and T50~378°C with 10% iron doping, and for SCS catalysts, they are T10~324°C and T50~372°C with 5% iron doping. It is noted that when doping ratio exceeded 20% for SCS catalysts, the catalyst activity greatly reduced (decreased by about 70°C). Comparing CP to SCS catalysts, it is interesting to find that SCS catalyst performed better than CP catalyst with low Fe doping (<5%) despite their lower surface area. However, this situation changed when Fe content increased from 10% to 30%, CP catalysts became better performing than SCS catalysts of the same composition. This makes the surface area not the determining factor for catalytic soot oxidation. Although this reaction is surface sensitive, what matters most is the contact between solid soot and catalyst particles, making the available surface for contact points become important. As seen from Table 1, the pore size of CP and SCS catalysts are around 3-5 nm, which is too small for soot particles (around 25 nm) to go through. Although SCS catalysts had a spongy structure with lower surface area, many openings (~250 nm) resulted from the combustion process could easily let soot particles penetrate in to increase the contact points and possibly provide more absorbed oxygen to the contact points and facilitate the oxygen diffusion through the catalyst [22]. But when the iron content exceeds 20%, the BET surface area for SCS catalysts degrade significantly (only 2-3 m^2g^{-1}). This makes the available contact points become very limited, resulting in a reduced activity performance.

Table 3. T10 and T50 for catalysts in tight contact condition

Tight	CeO_2	Fe_5Ce_{95}	$Fe_{10}Ce_{90}$	$Fe_{20}Ce_{80}$	$Fe_{30}Ce_{70}$	Printex-U
T10-CP(°C)	335.8±1.2	342.4±2.8	328.1±1.9	329.3±1.6	333.1±3.5	581±2.3
T10-SCS(°C)	328.7±2.5	323.6±1.7	336.0±1.2	396.8±2.4	400.9±3.7	581±2.3
T50-CP(°C)	393.1±0.7	400.2±1.3	377.5±2.0	388.5±1.1	396.4±1.0	649±3.1
T50-SCS(°C)	376.2±2.0	371.5±0.8	387.5±1.8	472.8±1.9	476.1±2.3	649±3.1

XRD results showed that Fe was successfully incorporated into CeO_2 lattice for both CP and SCS catalysts. For CP catalysts, the crystal size decreased with introduction of iron, implying that iron incorporation could inhibit crystal growth. In this way, the smaller crystal size and higher surface area can benefit oxygen diffusion and increase contact points. On the contrary, XRD pattern showed that crystal size grew with more Fe doping for SCS catalysts. Crystal growth can be an obstacle for good catalytic performance. The spherical structure of CP catalysts (shown in SEM image), resulting from the nucleation of the precipitates, can explain their higher surface area.

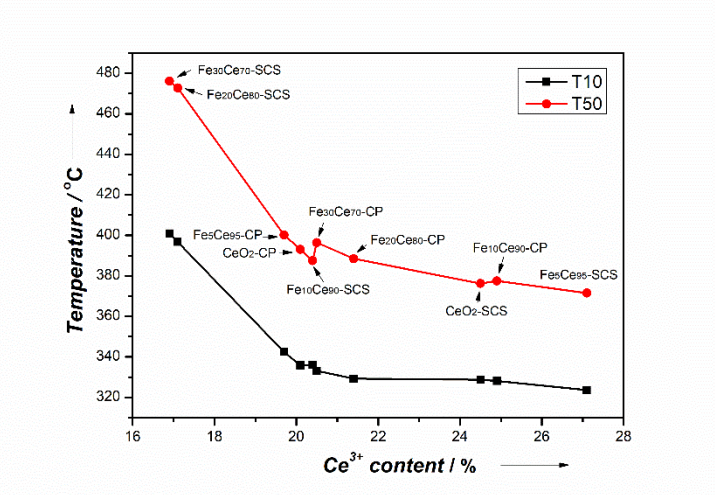

Peer-reviewed version available at Catalysts 2019, 9, 815; doi:10.3390/catal9100815

Figure 9. Relation between Ce^{3+} percentage and T10, T50

XPS results indicate that 10%-CP and 5%-SCS iron doping had the highest Ce^{3+} and O_α ratios on the surface among their own preparation method, which meant that the oxygen vacancies were maximized at these ratios. The trend of Ce^{3+} and O_α ratio follows the trend of T10 and T50, and hence follows the catalyst activity. Raman results and I_{596}/I_{463} values further confirmed oxygen vacancies, and $Fe_{10}Ce_{90}$-CP and Fe_5Ce_{95}-SCS showed highest oxygen vacancies within their own preparation method. Figure 9 shows the relation between Ce^{3+} percentage and T10, T50. It is noticed that the activity (trough T10 and T50) is really directly dependent on Ce^{3+}, irrespective of the preparation method. The ratio of Ce^{3+} can represent the availability of oxygen vacancies [47] as it is reported that higher Ce^{3+} concentration indicates more oxygen vacancies on the catalyst surface [15, 36, 38].Therefore, oxygen vacancies on the surface is found to be the determining factor for catalyst activity. With more Ce^{3+} or oxygen vacancy concentration, both T10 and T50 decreased in a similar fashion. Figure 9 shows that there is a threshold of around 20% Ce^{3+}, below which the catalyst activity rapidly deteriorates with further decreasing Ce^{3+} content, as indicated by the sharp drops in T10 and T50 at low Ce^{3+} content (T50: 476 to 393 °C). The samples with low Ce^{3+} also correspond to the lowest BET surface area (2-3 m^2g^{-1}), which could also contribute to the lower activity. However, because the catalytic soot oxidation involves contact between two solids, the BET surface area is less likely to play the most important role. Thus, the lower activities associated with $Fe_{20}Ce_{80}$-SCS and $Fe_{30}Ce_{70}$-SCS are attributed more to the low Ce^{3+} content than the low BET surface area. Above 20% Ce^{3+}, T10 and T50 would still decrease with increasing Ce^{3+} content, but at a much reduced rate (T50: 393 to 372 °C). This meant that Ce^{3+} content, and hence oxygen vacancy, has a great influence on catalyst activity. More oxygen vacancies facilitates adsorbing more oxygen species from gaseous oxygen, which then diffuse through the crystalline structure to the contact point between soot and catalyst and oxidize soot. Due to the existence of Ce^{3+} and Ce^{4+}, the reaction proceeds through redox mechanism. According to the mechanism study by Zhang et al. [20] redox cycle between Fe^{2+} and Fe^{3+} also participates in this soot oxidation and formed Fe-O-Ce bond, suggesting a synergetic effect of Fe and Ce interaction. When Fe^{3+} provided one O to oxidize soot, Fe^{3+} became Fe^{2+}. The Ce^{4+} on the neighboring site can supply one O to Fe^{2+}, changing it to Fe^{3+} through the reduction of Ce^{4+} to Ce^{3+}. Then absorbing one O from bulk could oxidize Ce^{3+} to Ce^{4+} again. The oxygen species are transferred within the catalyst lattice to reach the interface between soot and catalyst. The as-derived catalysts have different crystal structures due to various ratios of iron doping, which can cause lattice distortion and surface defects, thus changing the bond between Ce and O and creating some oxygen vacancies on the catalyst surface. This is the reason why certain ratios of iron doping can improve the catalyst activity.

H_2-TPR results showed that 10%-CP and 5%-SCS led to the highest reducibility, and therefore, highest activity, which is in agreement with XPS and Raman results. For SCS catalysts with iron doping, more bulk oxygen becomes releasable and can be more easily transferred to surface oxygen and oxidize soot. This makes the diffusion of bulk oxygen very important for SCS catalysts. However, for CP catalysts, the bulk oxygen reduction peaks were almost unchanged, implying that the Fe doping does cannot influence the bulk oxygen reduction.

Herein, the different activities of the as-produced catalysts were due to their different morphologies, lattice distortion and changed surface properties based on various iron doping. When the Fe doping ratio was lower than 5%, SCS catalysts showed better activity towards soot oxidation regardless of their low BET surface area. This is due to their porous structure, high surface oxygen vacancy concentration and better reducibility of surface oxygen. However, when the Fe doping ratio exceeds 10%, CP catalyst performed better, which can be attributed to their relative higher surface oxygen vacancies.

3. Materials and Methods

3.1. Preparation of the catalysts

Peer-reviewed version available at Catalysts 2019, 9, 815; doi:10.3390/catal9100815

Fe_xCe_{100-x}-CP (x = 5; 10; 20; and 30 in percent of molar ratio) catalysts were synthesized by co-precipitation (CP). A stoichiometric solution of iron nitrate nonahydrate (Sigma-Aldrich, CAS: 7782-61-8, 99.95% trace metals basis) and cerium nitrate hexahydrate (Sigma-Aldrich, CAS: 10294-41-4, 99.999% trace metals basis) were dissolved separately in deionized water, then mixed together with vigorous agitation. The aqueous ammonia (Sigma-Aldrich, CAS:1336-21-6, 28%-30% NH3 basis) was then gradually dropped into the above mentioned solution under stirring conditions until pH reached 8.5, after which the solution was aged in air for one day at room temperature with constant stirring. The resultant precipitates were separated by vacuum filtration with three washes with deionized water. The obtained precipitates were dried at 100°C for 12 h and then calcined at 500°C for 5h in static air. For comparison, pure cerium oxide - CeO_2 was prepared using a similar procedure.

Fe_xCe_{100-x}-SCS (x = 5; 10; 20; and 30 in percent of molar ratio) catalysts were obtained by solution combustion synthesis (SCS). An aqueous solution of iron nitrate nonahydrate (Sigma-Aldrich, CAS: 7782-61-8, 99.95% trace metals basis), cerium nitrate hexahydrate (Sigma-Aldrich, CAS: 10294-41-4, 99.999% trace metals basis) and glycine (Sigma-Aldrich, CAS: 56-40-6) in a stoichiometric ratio was prepared under vigorous stirring at 90°C to form the gel. Then, the gel was combusted on a heating plate. The combustion procedure is very fast, producing fine powders. The resultant sample was then calcined at 500°C for 5 h. CeO_2-SCS catalyst was developed using a similar procedure.

3.2. Characterization of the catalysts

X-ray powder diffraction (XRD) analysis was performed on X-ray powder diffractometer (German Bruker D4 (40 kV, 30 mA), with position-sensitive detector and CuKα radiation). The XRD patterns were recorded in steps of 0.01° with a scanning rate of 5°/min from 5° to 85°. The diffraction peaks were indexed according to the Powder Data File database (PDF 2004, International Centre of Diffraction Data, Pennsylvania).

The surface area was measured by means of N_2 adsorption-desorption isotherms using Beishide 3H-2000PS2 static volumetric method analyzer. The surface area of catalysts were evaluated by Brunauer-Emmett-Teller (BET) method.

The morphologies, microstructures and elemental composition of the obtained catalysts were characterized by a Field-emission scanning electron microscope (FE-SEM, Zeiss MERLIN with Gemini-II column).

X-ray photoelectron spectroscopy (XPS) measurements were carried out on ESCALab220i-XL electron spectrometer (VG Scientific Ltd, UK) with 300 W AlKα X-ray source equipment to investigate the oxidation states of cerium and iron, and availability of oxygen on catalyst surface. The calibration of binding energies was conducted by using C1s peaks at 284.8eV. Spectra-fits were performed with Gaussian-Lorentzian functions by using CasaXPS software.

The Raman spectra of the catalysts were measured on a Renishaw InVia micro laser Raman spectrometer (Renishawplc, Wottonunder-Edge, UK) with a 4mW Ar+ laser source (λex = 532nm) with a cooled CCD detector at room temperature to differentiate chemical structures. The acquisition time was 60s and the scanning range was 100-800cm^{-1}.

Temperature-programmed reduction with H_2 (H_2-TPR) experiments was carried out to study the reducibility of the catalyst by using a Micromeritics Autochem II 2920 analyzer with a thermal conductivity detector (TCD). 50mg catalyst was first pre-treated at 150°C for 1h under 40ml/min N_2 flow to remove water and other contaminants and then cooled down to room temperature. TPR analysis was conducted by heating up the sample to 700°C at 10°C /min in a flow of 40 ml/min 10% H_2/Ar.

3.3. Catalytic activity tests

Thermogravimetric analysis (TGA) of catalytic soot oxidation were conducted on a TA Instrument Q500 apparatus to investigate catalytic activity. Printex-U carbon black, with particulate

Peer-reviewed version available at Catalysts 2019, 9, 815; doi:10.3390/catal9100815

size of 25 nm and 100 m^2g^{-1} surface area, was used as model of soot. Tight contact condition of mixed sample was obtained by grinding soot and catalyst with a weight ratio of 1:9 in an agate mortar for 10 minutes. For each TGA test, a weighted amount of 10 mg sample was pre-treated at 150°C under 60 ml/min Nitrogen for 30 min to remove water and other contaminants. Then, the sample was heated up to 800°C under 40 ml/min air with a heating rate of 10°C /min. The thermogravimetric curves were obtained by continuously recording the mass change, along with increased temperature. Each TGA test was repeated three times to ensure the repeatability of the results. The activity of catalyst was evaluated by T10 and T50. T10 is commonly used as the ignition temperature, which is the temperature at 10% conversion of soot [1, 20, 22, 49]. T50 is the combustion temperature, identified as the temperature when 50% of soot is oxidized [1, 2, 22, 49].

5. Conclusions

Distinct morphologies of iron doped ceria catalyst with different Fe doping ratios were prepared by co-precipitation and solution combustion methods, for catalyzing soot oxidation. It was confirmed by XRD that iron was incorporated in the cerium oxide lattice, which formed a solid solution. The main conclusions of this study are:

- Irrespective of the fabrication method, the most important parameter that dictates the reaction activity (e.g. T50) is the Ce^{3+} content, which is closely related to the content of oxygen vacancies.
- The activity increases notably when Ce^{3+} content increases up to 20% (T50 from 476 °C at 17% Ce^{3+} down to 393 °C at 20% Ce^{3+}). Above 20% Ce^{3+} content, the activity increases moderately (T50 of 372 °C at 27% Ce^{3+}).
- For both fabrication methods, there is an optimum Fe content that gives the highest activity. For SCS catalyst, the optimum Fe content is 5%, and for CP catalyst, it is 10%.
- The pore size is mostly about 3-5 nm (both CP and SCS), which is much smaller than the 25 nm soot particles used here. This is why, although the BET surface area is greater for CP than SCS, it has only moderate effect on the activity.
- The catalyst preparation method has a profound impact on the catalyst morphology. The CP catalyst shows dense spherical morphology, whereas the SCS catalyst has a spongy structure with large openings, around 250 nm, which can be large enough for soot particles to penetrate in and contact with the catalyst. Therefore, it can be anticipated that more soot particle can deposit on the SCS catalyst.

Author Contributions: Li prepared the samples, conducted the experiments, analyzed the data and wrote this paper. Wen and Croiset led and oversaw the University of Waterloo part of this work - specifically the catalyst fabrication and experiments. Raj provided initial consultants.

Acknowledgments: Natural Sciences and Engineering Research Council of Canada (NSERC) and BioFuelNet Canada are acknowledged for sponsoring this research project. The authors would also thank the Key Laboratory of Coal Science and Technology at Taiyuan University of Technology for helping characterize the catalysts using Raman and H_2-TPR spectroscopy.

Conflicts of Interest: The authors declare no conflict of interest.

References

1. T. Andana, M. Piumetti, S. Bensaid, N. Russo, D. Fino, R. Pirone, Nanostructured ceria-praseodymia catalysts for diesel soot combustion, Applied Catalysis B: Environmental, 197 (2016) 125-137.
2. P. Venkataswamy, D. Jampaiah, K.N. Rao, B.M. Reddy, Nanostructured Ce0.7Mn0.3O2−δ and Ce0.7Fe0.3O2−δ solid solutions for diesel soot oxidation, Applied Catalysis A: General, 488 (2014) 1-10.
3. A.C. Lluís Soler, Carlos Escudero, Virginia PØrez-Dieste, Eleonora Aneggi, Alessandro Trovarelli, and Jordi Llorca, Ambient pressure photoemission spectroscopy reveals the mechanism of carbon soot oxidation in ceria-based catalysts, ChemCatChem, 8 (2016) 2748 – 2751.
4. A. Bueno-López, Diesel soot combustion ceria catalysts, Applied Catalysis B: Environmental, 146 (2014) 1-11.

Peer-reviewed version available at Catalysts 2019, 9, 815; doi:10.3390/catal9100815

5. D. Fino, S. Bensaid, M. Piumetti, N. Russo, A review on the catalytic combustion of soot in Diesel particulate filters for automotive applications: From powder catalysts to structured reactors, Applied Catalysis A: General, 509 (2016) 75-96.
6. C.A. Neyertz, E.D. Banús, E.E. Miró, C.A. Querini, Potassium-promoted Ce0.65Zr0.35O2 monolithic catalysts for diesel soot combustion, Chemical Engineering Journal, 248 (2014) 394-405.
7. J. Oi-Uchisawa, A. Obuchi, S. Wang, T. Nanba, A. Ohi, Catalytic performance of Pt/MOx loaded over SiC-DPF for soot oxidation, Applied Catalysis B: Environmental, 43 (2003) 117-129.
8. J.P.A. Neeft, M. Makkee, J.A. Moulijn, Diesel particulate emission control, Fuel Processing Technology, 47 (1996) 1-69.
9. R. Burch, Knowledge and Know-How in Emission Control for Mobile Applications, Catalysis Reviews, 46 (2004) 271-334.
10. A. Russell, W.S. Epling, Diesel Oxidation Catalysts, Catalysis Reviews, 53 (2011) 337-423.
11. P. Eastwood, Critical topics in exhaust gas aftertreatment, 2000.
12. A. Bueno-López, K. Krishna, B. van der Linden, G. Mul, J.A. Moulijn, M. Makkee, On the mechanism of model diesel soot-O2 reaction catalysed by Pt-containing La3+-doped CeO2: A TAP study with isotopic O2, Catalysis Today, 121 (2007) 237-245.
13. Y. Nagai, T. Hirabayashi, K. Dohmae, N. Takagi, T. Minami, H. Shinjoh, S.i. Matsumoto, Sintering inhibition mechanism of platinum supported on ceria-based oxide and Pt-oxide–support interaction, Journal of Catalysis, 242 (2006) 103-109.
14. Y. Wei, Z. Zhao, J. Liu, C. Xu, G. Jiang, A. Duan, Design and Synthesis of 3D Ordered Macroporous CeO2-Supported Pt@ CeO2-δ Core–Shell Nanoparticle Materials for Enhanced Catalytic Activity of Soot Oxidation, Small, 9 (2013) 3957-3963.
15. S. Liu, X. Wu, D. Weng, R. Ran, Ceria-based catalysts for soot oxidation: a review, Journal of Rare Earths, 33 (2015) 567-590.
16. M. López-Haro, J. Pérez-Omil, J. Hernández-Garrido, S. Trasobares, A. Hungría, J. Cíes, P. Midgley, P. Bayle-Guillemaud, A. Martínez-Arias, S. Bernal, Advanced Electron Microscopy Investigation of Ceria–Zirconia-Based Catalysts, ChemCatChem, 3 (2011) 1015-1027.
17. R. Kopelent, J.A. van Bokhoven, J. Szlachetko, J. Edebeli, C. Paun, M. Nachtegaal, O.V. Safonova, Catalytically active and spectator Ce3+ in ceria-supported metal catalysts, Angewandte Chemie International Edition, 54 (2015) 8728-8731.
18. M. Shelef, R.W. McCabe, Twenty-five years after introduction of automotive catalysts: what next?, Catalysis Today, 62 (2000) 35-50.
19. R.M. Heck, R.J. Farrauto, Automobile exhaust catalysts, Applied Catalysis A: General, 221 (2001) 443-457.
20. Z. Zhang, D. Han, S. Wei, Y. Zhang, Determination of active site densities and mechanisms for soot combustion with O2 on Fe-doped CeO2 mixed oxides, Journal of Catalysis, 276 (2010) 16-23.
21. A. Setiabudi, J. Chen, G. Mul, M. Makkee, J.A. Moulijn, CeO2 catalysed soot oxidation: The role of active oxygen to accelerate the oxidation conversion, Applied Catalysis B: Environmental, 51 (2004) 9-19.
22. P. Miceli, S. Bensaid, N. Russo, D. Fino, Effect of the morphological and surface properties of CeO2-based catalysts on the soot oxidation activity, Chemical Engineering Journal, 278 (2015) 190-198.
23. J. Liu, Z. Zhao, J. Wang, C. Xu, A. Duan, G. Jiang, Q. Yang, The highly active catalysts of nanometric CeO2-supported cobalt oxides for soot combustion, Applied Catalysis B: Environmental, 84 (2008) 185-195.
24. H. Muroyama, S. Hano, T. Matsui, K. Eguchi, Catalytic soot combustion over CeO2-based oxides, Catalysis Today, 153 (2010) 133-135.
25. X. Li, S. Wei, Z. Zhang, Y. Zhang, Z. Wang, Q. Su, X. Gao, Quantification of the active site density and turnover frequency for soot combustion with O2 on Cr doped CeO2, Catalysis Today, 175 (2011) 112-116.
26. H. Li, K. Li, H. Wang, X. Zhu, Y. Wei, D. Yan, X. Cheng, K. Zhai, Soot combustion over Ce1-xFexO2-δ and CeO2/Fe2O3 catalysts: Roles of solid solution and interfacial interactions in the mixed oxides, Applied Surface Science, 390 (2016) 513-525.
27. J.M. Thomas, R. Raja, Mono-, Bi- and Multifunctional Single-Sites: Exploring the Interface Between Heterogeneous and Homogeneous Catalysis, Topics in Catalysis, 53 (2010) 848-858.
28. K. An, G.A. Somorjai, Nanocatalysis I: Synthesis of Metal and Bimetallic Nanoparticles and Porous Oxides and Their Catalytic Reaction Studies, Catalysis Letters, 145 (2015) 233-248.

Peer-reviewed version available at Catalysts 2019, 9, 815; doi:10.3390/catal9100815

29. S. Agarwal, L. Lefferts, B.L. Mojet, Ceria nanocatalysts: shape dependent reactivity and formation of OH, ChemCatChem, 5 (2013) 479-489.
30. Q. Yuan, H.-H. Duan, L.-L. Li, L.-D. Sun, Y.-W. Zhang, C.-H. Yan, Controlled synthesis and assembly of ceria-based nanomaterials, Journal of Colloid and Interface Science, 335 (2009) 151-167.
31. Y. Wei, Z. Zhao, X. Yu, B. Jin, J. Liu, C. Xu, A. Duan, G. Jiang, S. Ma, One-pot synthesis of core-shell Au@CeO2-[small delta] nanoparticles supported on three-dimensionally ordered macroporous ZrO2 with enhanced catalytic activity and stability for soot combustion, Catalysis Science & Technology, 3 (2013) 2958-2970.
32. Y. Wei, Z. Zhao, J. Liu, C. Xu, G. Jiang, A. Duan, Design and Synthesis of 3D Ordered Macroporous CeO 2 -Supported Pt@CeO 2-δ Core-Shell Nanoparticle Materials for Enhanced Catalytic Activity of Soot Oxidation, 2013.
33. Y. Wei, J. Liu, Z. Zhao, A. Duan, G. Jiang, The catalysts of three-dimensionally ordered macroporous Ce1−xZrxO2-supported gold nanoparticles for soot combustion: The metal–support interaction, Journal of Catalysis, 287 (2012) 13-29.
34. G. Zhang, Z. Zhao, J. Liu, G. Jiang, A. Duan, J. Zheng, S. Chen, R. Zhou, Three dimensionally ordered macroporous Ce1-xZrxO2 solid solutions for diesel soot combustion, Chemical Communications, 46 (2010) 457-459.
35. S. Bensaid, N. Russo, D. Fino, CeO2 catalysts with fibrous morphology for soot oxidation: The importance of the soot–catalyst contact conditions, Catalysis Today, 216 (2013) 57-63.
36. M. Piumetti, S. Bensaid, N. Russo, D. Fino, Nanostructured ceria-based catalysts for soot combustion: Investigations on the surface sensitivity, Applied Catalysis B: Environmental, 165 (2015) 742-751.
37. P. Palmisano, N. Russo, P. Fino, D. Fino, C. Badini, High catalytic activity of SCS-synthesized ceria towards diesel soot combustion, Applied Catalysis B: Environmental, 69 (2006) 85-92.
38. H. Wang, S. Luo, M. Zhang, W. Liu, X. Wu, S. Liu, Roles of oxygen vacancy and Ox− in oxidation reactions over CeO2 and Ag/CeO2 nanorod model catalysts, Journal of catalysis, 368 (2018) 365-378.
39. L. Katta, P. Sudarsanam, G. Thrimurthulu, B.M. Reddy, Doped nanosized ceria solid solutions for low temperature soot oxidation: Zirconium versus lanthanum promoters, Applied Catalysis B: Environmental, 101 (2010) 101-108.
40. D. Harshini, D.H. Lee, J. Jeong, Y. Kim, S.W. Nam, H.C. Ham, J.H. Han, T.-H. Lim, C.W. Yoon, Enhanced oxygen storage capacity of Ce0. 65Hf0. 25M0. 1O2-δ (M= rare earth elements): Applications to methane steam reforming with high coking resistance, Applied Catalysis B: Environmental, 148 (2014) 415-423.
41. E. Lim, Y.J. Kim, J.H. Kim, T. Ryu, S. Lee, B.K. Cho, I.-S. Nam, J.W. Choung, S. Yoo, NO oxidation activity of Ag-doped perovskite catalysts, Journal of catalysis, 319 (2014) 182-193.
42. B. Liu, C. Li, G. Zhang, X. Yao, S.S. Chuang, Z. Li, Oxygen vacancy promoting dimethyl carbonate synthesis from CO2 and methanol over Zr-doped CeO2 nanorods, ACS Catalysis, 8 (2018) 10446-10456.
43. Y. Tang, H. Qiao, H. Wang, P. Tao, Nanoparticulate Mn0.3Ce0.7O2: a novel electrocatalyst with improved power performance for metal/air batteries, Journal of Materials Chemistry A, 1 (2013) 12512-12518.
44. T.R. Sahoo, M. Armandi, R. Arletti, M. Piumetti, S. Bensaid, M. Manzoli, S.R. Panda, B. Bonelli, Pure and Fe-doped CeO2 nanoparticles obtained by microwave assisted combustion synthesis: Physico-chemical properties ruling their catalytic activity towards CO oxidation and soot combustion, Applied Catalysis B: Environmental, 211 (2017) 31-45.
45. N. RĂDUȚOIU, C. TEODORESCU, SATELLITES IN Ce 3d X-RAY PHOTOELECTRON SPECTROSCOPY OF CERIA, Digest Journal of Nanomaterials & Biostructures (DJNB), 8 (2013).
46. P. Sudarsanam, B. Mallesham, D.N. Durgasri, B.M. Reddy, Physicochemical characterization and catalytic CO oxidation performance of nanocrystalline Ce–Fe mixed oxides, RSC Advances, 4 (2014) 11322-11330.
47. D. Jampaiah, K.M. Tur, S.J. Ippolito, Y.M. Sabri, J. Tardio, S.K. Bhargava, B.M. Reddy, Structural characterization and catalytic evaluation of transition and rare earth metal doped ceria-based solid solutions for elemental mercury oxidation, RSC Advances, 3 (2013) 12963-12974.
48. W. Wang, Q. Zhu, F. Qin, Q. Dai, X. Wang, Fe doped CeO2 nanosheets as Fenton-like heterogeneous catalysts for degradation of salicylic acid, Chemical Engineering Journal, 333 (2018) 226-239.
49. M. Piumetti, S. Bensaid, N. Russo, D. Fino, Investigations into nanostructured ceria–zirconia catalysts for soot combustion, Applied Catalysis B: Environmental, 180 (2016) 271-282.

Peer-reviewed version available at *Catalysts* **2019**, *9*, 815; doi:10.3390/catal9100815

522 **Table of Contents**

523

FULL PAPER

This study investigates oxygen vacancy's role in Fe-doped CeO_2 for catalytic soot oxidation. 10% and 5% Fe contents yielded the highest activity for co-precipitation and solution combustion synthesis catalysts, respectively. Regardless of the fabrication method, Ce^{3+} content, related to oxygen vacancies, plays the most important role in affecting the activity.

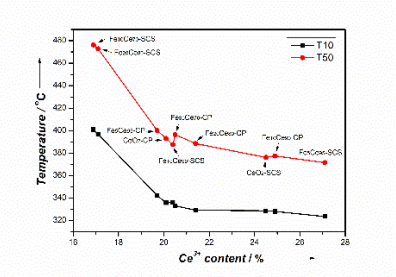

*Boyu Li, John Z. Wen, Abhishek Raj, Eric Croiset**

Reactive Fe-O-Ce Sites in Ceria Catalysts for Soot Oxidation

524